Calorimetry of a phase slip in a Josephson junction

E. Gümüş ⊕[1], D. Majidi ⊕[1], D. Nikolić[2], P. Raif ⊕[1,2], B. Karimi ⊕[3], J. T. Peltonen ⊕[3], E. Scheer ⊕[2], J. P. Pekola[3], H. Courtois ⊕[1], W. Belzig ⊕[2] & C. B. Winkelmann ⊕[1] ✉

Josephson junctions are a central element in superconducting quantum technology; in these devices, irreversibility arises from abrupt slips of the quantum phase difference across the junction. This phase slip is often visualized as the tunnelling of a flux quantum in the transverse direction to the superconducting weak link, which produces dissipation. Here we detect the instantaneous heat release caused by a phase slip in a Josephson junction, signalled by an abrupt increase in the local electronic temperature in the weak link and subsequent relaxation back to equilibrium. Beyond the advance in experimental quantum thermodynamics of observing heat in an elementary quantum process, our approach could allow experimentally investigating the ubiquity of dissipation in quantum devices, particularly in superconducting quantum sensors and qubits.

The magnetic flux threading a superconducting loop is quantized in units of the flux quantum as $\Phi_0 = h/2e$ (h, the Planck constant; e, the elementary charge). The tunnelling of a flux quantum in or out of such a loop is associated to a change of 2π in the winding of the phase of the quantum wavefunction along the loop. The manipulation of an individual flux quantum is at the core of superconducting circuit logic, in both classical and quantum information regime[1–3]. Rapid single-flux quantum logic can operate up to 100 GHz frequencies and is considered as promising classical control electronics of qubits[4–6]. In the quantum regime, the coherent superposition and manipulation of flux states is at the basis of flux qubits[7,8] and the fluxonium[9,10].

Slips of the quantum phase occur when the gauge-invariant phase difference across a weak link, that is, a Josephson junction, in the superconducting loop suddenly relaxes (Fig. 1). Quantum phase slips are ubiquitous in superconducting electronics and can be seen as the dual process to Cooper-pair tunnelling. Furthermore, coherent quantum phase slips have been proposed as a building block for phase-slip qubit devices[1,2,11] and quantum current metrology applications[12]. On the other hand, the proliferation of phase slips is responsible for the destruction of superconductivity in one dimension[13] and can lead to thermal avalanches in current-biased Josephson junctions[14]. In essence, a phase slip, which can also be viewed as the transverse tunnelling of a flux quantum (Fig. 1a), is the most elementary dissipative process in coherent superconducting electronics.

In this work, we investigate the thermal signature of individual phase slips in a superconducting Josephson junction. Applying a MHz-bandwidth electron thermometry technique to a superconducting quantum interference device (SQUID), we measure the heat generated by a single phase slip as well as the subsequent thermal relaxation. The data are in good agreement with a theoretical model that we developed for describing the superconducting properties of the device. Our work, therefore, demonstrates the possibility to quantitatively account for dissipative effects—in real time—in quantum nanoelectronics, with evident applications to quantum computing.

The experimental core element is a SQUID, that is, a superconducting loop containing one (as is the case here) or more Josephson junctions, and to which a magnetic flux Φ_x is applied. The difference between the applied and physical flux is absorbed by screening supercurrents, leading to a gradient in the phase of the quantum wavefunction along the loop and—to a large extent—across the Josephson weak link. The relation between Φ_x and phase drop φ across the Josephson junction can be written as

$$2\pi(\Phi_x/\Phi_0) = \varphi + \beta\sin(\varphi), \tag{1}$$

where the screening parameter $\beta = 2\pi L I_c/\Phi_0$, L is the loop inductance and I_c the Josephson junction's critical current[15]. Irreversibility arises when the SQUID's magnetic screening parameter β exceeds 1 and

[1]Univ. Grenoble Alpes, CNRS, Grenoble INP, Institut Néel, Grenoble, France. [2]Fachbereich Physik, Universität Konstanz, Konstanz, Germany. [3]QTF Centre of Excellence, Department of Applied Physics, Aalto University School of Science, Aalto, Finland. ✉e-mail: clemens.winkelmann@neel.cnrs.fr
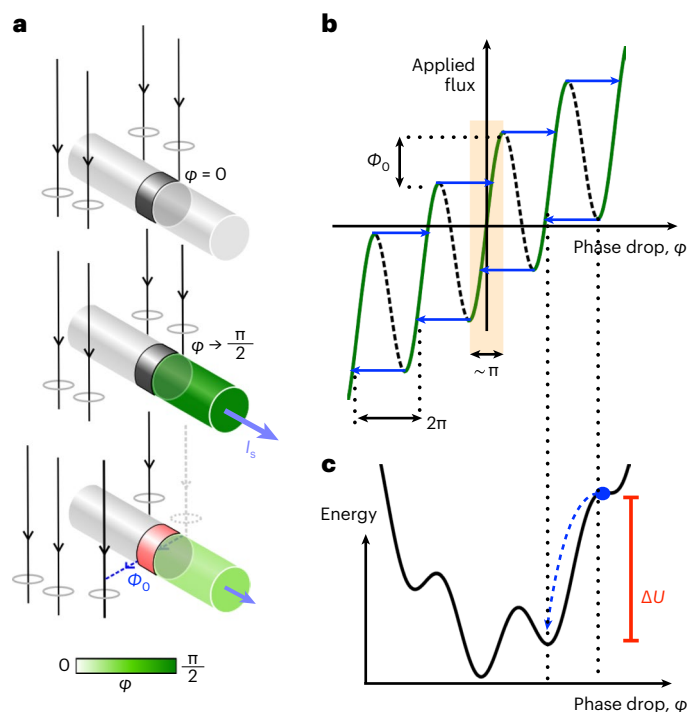
Fig. 1 | Phase slip in a hysteretic Josephson junction. a, Real-space sketch of the phase-slip mechanism: at the instability point of the $\Phi_x(\varphi)$ relation, the phase drop φ and the screening current I_s abruptly relax to smaller values, as a quantum of flux tunnels perpendicular to the Josephson junction (dark grey), releasing heat. **b**, Phase drop φ across the SNS junction versus applied flux to the SQUIPT, as per equation (1) with $\beta = 10$. The dashed part of the curve cannot be accessed. In a quantum phase slip (blue arrows), φ changes by slightly less than 2π. **c**, Potential energy of the SQUIPT as a function of φ. A local energy minimum can become unstable as the externally applied flux is changed. By macroscopic quantum tunnelling of the phase, a lower energy valley is reached, releasing an energy ΔU.

equation (1) is no longer single valued (Fig. 1b,c). In this situation, the penetration of an additional flux quantum into the SQUID loop does not occur smoothly and reversibly, but via a sudden jump of the phase, that is, a phase slip.

The above concepts are the basis of extensive applications in superconducting electronics, such as SQUID magnetometry and superconducting flux qubits[7,16,17]. Notably, the Josephson weak links used in such SQUIDs can be provided by a variety of junction types, including tunnel junctions, microbridges and proximity weak links[18]. In the latter, a short, non-intrinsically superconducting element, such as a normal metallic wire allows for superconducting correlations to propagate between both superconducting reservoirs. Due to the wire's usually low normal-state resistance, following the resistively and capacitively shunted Josephson junction model, the quantum phase dynamics in such superconductor–normal metal–superconductor (SNS) Josephson junctions are inherently overdamped[15]. This ensures that on a phase slip, the quantum phase only evolves towards the nearest-neighbouring potential valley (Fig. 1c). This releases an energy of

$$\Delta U = \frac{\Phi_0}{2\pi L} \int \Phi_x \, d\varphi, \qquad (2)$$

which depends on the magnitude of the quantum phase slip. In the large-β limit, the phase jumps by about 2π, and $\Delta U \approx I_c \Phi_0$.

Our device consists of a SQUID with a single Josephson junction, provided by an SNS weak link of length 520 nm (Fig. 2a). Here the superconducting circuit parts are made of Al, whereas metal N is made of copper. Although the loop is grounded, the centre of N

is further contacted by another superconducting finger through a tunnel junction (Fig. 2a), with normal-state resistance $R_T \approx 7$ kΩ. This SQUID variant was named SQUIPT[19], where PT stands for proximity transistor. Our SQUIPT was designed to be in the hysteretic regime. For this, we took into account the geometric and kinetic inductance contributions, leading to $L \approx 630 \pm 50$ pH. The critical current I_c of the SNS junction cannot be independently determined in this device, but is expected from similar SNS devices in a current-biased geometry to be of a few microamperes[20–22]. From this, values of the screening parameter $\beta \approx 10$ can be anticipated, in good agreement with experiments, as discussed below.

Applying a d.c. voltage V_b to the tunnel junction, we can perform tunnel spectroscopy by measuring its differential conductance $G(V_b)$. Here G is not read out, as usual, by a low-frequency transport measurement, but by a radio-frequency (RF) technique, using a superconducting LC resonator with resonant frequency $f_0 = 575$ MHz (refs. [23–25]). By embedding the tunnel junction in parallel to the resonator, and for a fixed incident RF power P_{in}, changes in G can be read out by their effect on the transmitted power at resonance P_{out}, which we record after cryogenic amplification (Supplementary Section II). This has the paramount advantage of allowing for extremely rapid measurements, limited by the resonator bandwidth, of about 10 MHz here. The experimental noise floor is determined by the thermal input noise of the commercial cryogenic microwave amplifier, with a noise temperature of about 6 K near f_0.

Figure 2b shows the measurements of $P_{out}(V_b)$ at two temperatures. Several characteristic spectroscopic features stand out, particularly (1) a spectroscopic gap with a total width of 480 µV, (2) subgap resonances near ±190 µV visible only at 400 mK and (3) three low-energy resonances at 0 and ±15 µV. Keeping in mind that the tunnel junction connects an intrinsic superconductor with gap Δ and a proximized metal with a (smaller) induced gap E_g, we can evaluate the total spectroscopic gap as $2(\Delta + E_g)/e$. At intermediate temperatures, thermally activated conductance resonances occur at $\pm|\Delta - E_g|/e$, which we identify as feature (2) mentioned above. From the two above relations, we find a gap $\Delta = 210 \pm 5$ µeV in the superconducting probe electrode at 400 mK (225 µeV at 50 mK), a typical value in nanostructured Al. We further extract $E_g = 29$ µeV, in good agreement with theoretical estimates (Supplementary Section VI). Eventually, the conductance resonance at $V_b = 0$ (feature (3) above) is a signature of Josephson coupling across the tunnel junction, which was purposely designed to have an intermediate transparency, to act as an ultrasensitive probe of the electron temperature in N (ref. [25] and Supplementary Section VII). The satellite peaks at ±15 µV are probably the signature of inelastic Cooper-pair tunnelling[25] and are not of central relevance to this work.

As visible in Fig. 2b,c and already discussed in detail in refs. [25–27], the zero-bias conductance of the tunnel junction and therefore $P_{out}(V_b = 0)$ is a sensitive probe of the electron temperature T in N. Accordingly, we set $V_b = 0$ in the remainder of this work and use P_{out} for both static and dynamic electron thermometry, after initial calibration under equilibrium conditions (Fig. 2c). However, and in contrast to previous work[25–27] in which N was not subject to a phase drop, in the present device, the tunnel junction conductance and thus P_{out} are clearly also a function of phase φ across the SNS junction. This is shown in Fig. 2d, where sweeping the applied flux translates into a phase variation via equation (1). As $\varphi \to \pi/2$, the decrease in E_g (refs. [28,29]) entails a rapidly shrinking Josephson energy E_J of the tunnel junction and thus a decrease in $G(0)$, that is, an increase in P_{out}. When the switching point in the $\Phi_x(\varphi)$ relation is reached, φ suddenly relaxes to a smaller value (modulo 2π), restoring E_J and thus leading to an abrupt drop in P_{out}. As expected, the same pattern is repeated with period Φ_0 in the applied flux and mirror symmetric under inversion of the sweep direction[30]. At higher temperatures, $\beta \propto I_c$ decreases and the modulation amplitude of $P_{out}(\Phi_x)$ shrinks, whereas the Φ_0 periodicity of the signal is preserved.
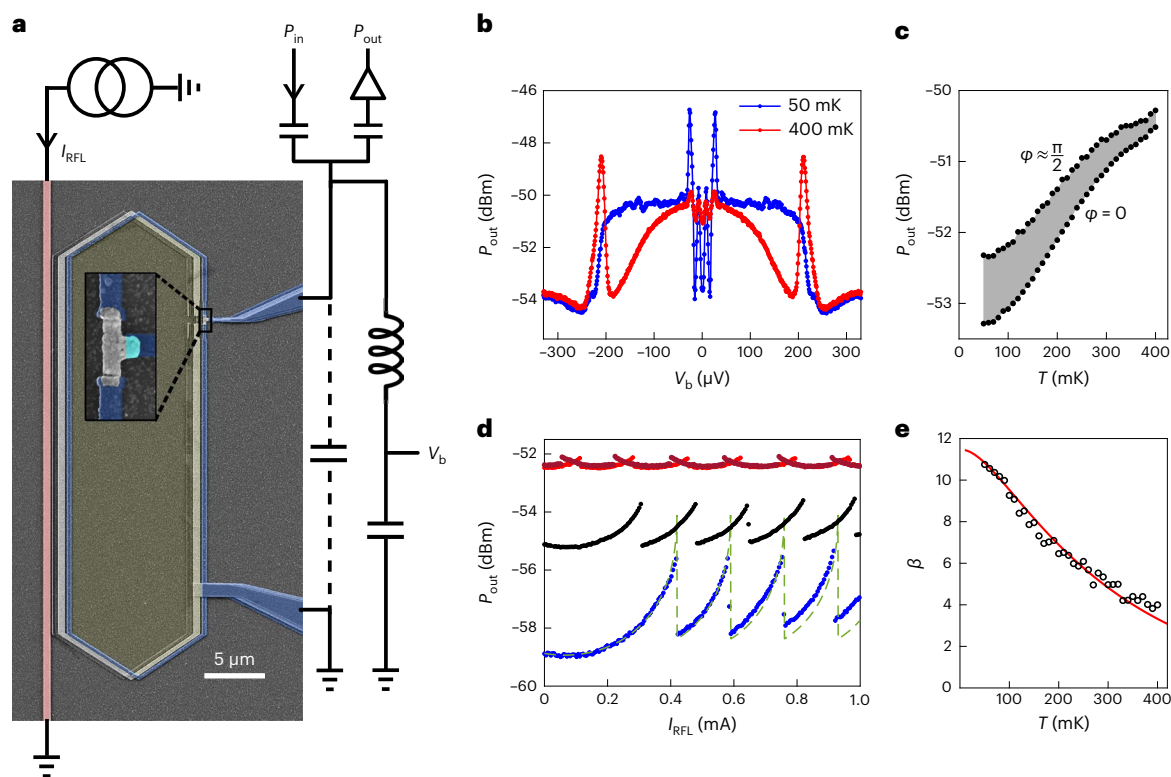
Fig. 2 | Hysteretic RF-SQUIPT. a, Device schematic, including a false-colour scanning electron micrograph (scale bar, 5 μm) of the SQUIPT loop (yellow area) and the RFL (pink). The zoomed-in view highlights the SNS junction (Al, blue; Cu, grey), laterally connected by the tunnel contact (cyan) (scale bar, 200 nm), connected to the resonator. **b**, Bias spectroscopy $P_{out}(V_b)$ at cryostat temperatures of 50 mK (blue) and 400 mK (red). Here $P_{out} \approx -50.4$ dBm corresponds to $G = 0$ and $P_{out} = -54$ dBm corresponds to $G \approx 1/R_T$. **c**, Calibration of $P_{out}(V_b = 0)$ versus cryostat temperature at equilibrium, under two different phase

drops. The grey-shaded region, thus, covers all the possible values of $P_{out}(T, \varphi)$. **d**, Resonator response at $V_b = 0$ as a function of increasing applied magnetic flux, at three cryostat temperatures (50 mK, blue; 200 mK, black; 400 mK, red). The dark-red line exemplifies the response to a downward sweep of flux. The dashed line is a calculation (see the main text). **e**, Temperature dependence of the screening parameter β, extracted from **d**, and the theoretical fit (red line; see the main text).

For a quantitative understanding of RF-SQUIPT, we use the quasi-classical Usadel equations[28,31–33], with a single consistent set of microscopic parameters (Supplementary Section VI). The density of states in N is known to display a minigap, which approximately depends on φ like $E_g(\varphi) = E_g(0)|\cos(\varphi/2)|$ (ref. [28]). The tunnel junction connecting the condensate in N to the superconducting probe electrode has a Josephson energy $E_J(\varphi, T)$ and thus a zero-bias conductance $G(\varphi, T)$, which can be analytically drawn back to $E_g(\varphi)$ and the critical current I_c of the SNS junction. In combination with equation (1) and the relation between G and P_{out}, the calculation provides an accurate description of the applied-flux dependence of the RF signal (Fig. 2d), the only adjustable parameter being the magnitude of β.

The temperature dependence of β extracted from the data in Fig. 2d is plotted in Fig. 2e, following the trend expected for $I_c(T)$ in an SNS junction. The solid line shows the calculation from the same model as above, yielding a 5.9 μA zero-temperature critical current in the SNS junction. The parameters entering the calculation, particularly the minigap, are independently determined using the tunnel spectra (Fig. 2b). We attribute the slight underestimation of β by theory above 300 mK to the temperature dependence of the kinetic inductance, which was not accounted for here.

The data discussed so far, and summarized in Fig. 2, provide a consistent physical understanding of the RF-SQUIPT under time-averaged—and thus isothermal—conditions. We now move to the time-resolved response $P_{out}(t)$, which displays the calorimetric signature of the heat deposited by individual phase-slip events. In addition to the static flux bias, we apply a time-dependent (square-wave or pulsed) flux by

passing a current $I_{RFL}(t)$ through the superconducting rapid flux line (RFL), visible on the left side of the SQUIPT (Fig. 2a). The instantaneous flux bias is $\Phi_x(t) = MI_{RFL}(t)$, with a mutual inductance $M = 12.1$ pH (Supplementary Section I). To increase the signal-to-noise ratio, we average the resonator response over a large number of periodically generated identical 70 ns flux pulses.

As long as the amplitude of the flux pulses does not exceed the threshold leading to a phase slip, P_{out} instantaneously follows changes in $\Phi_x(t)$ (Supplementary Fig. 6). However, as soon as the threshold to instability of the flux state is overcome, $P_{out}(t)$ displays, in addition, a slower relaxation to its novel equilibrium, which is indicative of thermalization. As evidenced from Fig. 3a, the relaxation dynamics after a flux pulse are strongly temperature dependent, as expected, for instance, from a dominantly electron–phonon (e–ph)-coupling-driven thermalization after an initial heating event[24]. Above 300 mK, the relaxation times become too short (<1 μs) to be measured.

The thermal dynamics can be described by a heat balance equation, based on the standard assumption that variations in the absorber's internal energy U are evacuated to a heat bath via e–ph coupling. In metallic nanostructures at low temperatures, this power is usually written as $\dot{Q}_{e-ph} = \Sigma \mathcal{V}(T^n - T_0^n)$, where $n \approx 5$, $\Sigma \approx 2 \times 10^9$ W K^{-5} m^{-3} is the e–ph coupling constant in copper[34,35] and $\mathcal{V} \approx 8 \times 10^{-21}$ m^{-3} is the geometrically estimated absorber volume. Given the rather small E_g in the SNS junction, our calculations indicate that the proximity effect should only lead to negligibly small (<10%) departures from the normal-state e–ph coupling and heat capacity C, at the experimental temperatures (Supplementary Section VI). Therefore, we write $U = \gamma T^2/2$, using a
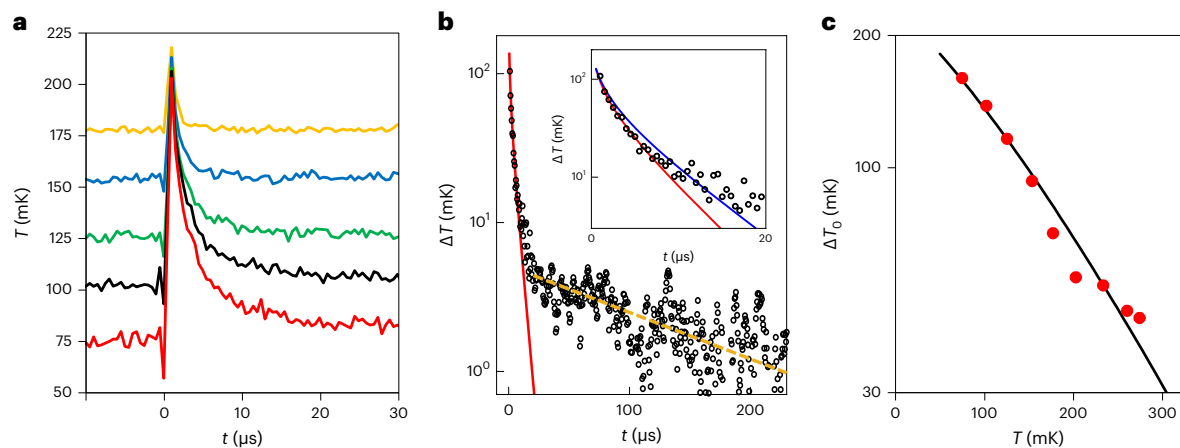
Fig. 3 | Heat relaxation dynamics after a phase slip. a, Time-resolved electron temperature in the absorber, at different starting temperatures set by the cryostat bath, following a 70 ns flux pulse at $t = 0$. The data-sampling rate is 2 MHz; the data shown are the result of averaging over 10^5 pulses at a repetition rate of 2 kHz. **b**, Return to equilibrium $\Delta T(t)$ at 100 mK, following a flux pulse. Same data as the black curve in **a**, but in a semilog-scale representation and over a wider time window. The red line is a calculation based on the model discussed in the main text, with $n = 4.85$. The inset shows a zoomed-in view on the short time response, with a comparison to the model using two values of $n = 4.85$ (red) and 5.00 (blue). The dashed line is an exponential fit (with time constant $\tau \approx 140\ \mu\text{s}$) to the long-term relaxation, evidencing the presence of a second slowly relaxing bath. **c**, Magnitude of the initial temperature rise ΔT_0 at $t = 0$, determined by the fit as shown in **b** (bullets). The solid line is a calculation (see the main text).

reported value of $\gamma = 71\ \text{J m}^{-3}\ \text{K}^{-2}$ in nanostructured Cu (ref.[35]). As shown in Fig. 3a, the temperature increase after the initial heat pulse can be large compared with the starting temperature. The dynamical heat-balance differential equation, thus, cannot be linearized in $\Delta T = T - T_b$, and must be numerically solved. The result at $T_b = 100$ mK is shown in Fig. 3b (red line), where $n = 4.85$ provides the best fit, leaving the initial temperature rise ΔT_0 as the only adjustable parameter. The calculation closely follows the data during the first period of thermal relaxation. Interestingly, the initial fast decay is rapidly taken over by a much slower process, which was already reported for nanoscale Cu absorbers[35,36]. This might be due to another heat reservoir, for instance, in surface states of the Cu absorber.

The initial temperature increase ΔT_0 after a flux pulse is plotted as a function of the starting temperature (Fig. 3c). Naturally, the temperature rise is the highest when starting from the lowest base temperature, because at a higher temperature, C increases and $\Delta U \approx I_c \Phi_0$ decreases. For quantitative modelling, one must bear in mind that a flux pulse necessarily induces two consecutive phase slips of opposite signs: one when ramping up the flux bias and the second when resetting the flux to its initial value. Details of the cascading of phase slips are discussed in Supplementary Section IV. Finally, assuming that the heat generated by the phase slips is fully released as quasiparticles in N, which relax via e–ph coupling, allows a very accurate description of both temperature relaxation dynamics and initial temperature rise ΔT_0 in N. The calculation of ΔT_0 (Fig. 3c, black line) is performed in the frame of the quasi-classical Usadel formalism with the same set of microscopic parameters as previously determined (Supplementary Section VI), in combination with equations (1) and (2) and the above-discussed heat balance model. The result is in excellent agreement with the data, without free parameters.

The observation of the heat deposited by the elementary dissipation process of hysteretic switching of flux states in quantum circuits highlights the paramount effect of dissipation in quantum circuits as well as the potential of large-bandwidth electron thermometry for quantum thermodynamics in nanoelectronic circuits. The use of lower-noise signal amplification schemes and absorbers with smaller heat capacity could allow lowering the calorimetric detection threshold by several orders of magnitude. Future experiments could aim, for instance, at detecting the minute dissipation arising from a

projective qubit measurement, with the tunnelling of a single electron, the emission of a single microwave photon[37] or the elusive axion with even smaller energy[38]. On the other hand, the proper measurement and control of dissipation in phase-slip-based circuits will allow for overcoming self-heating-limited device performances.

Online content

Any methods, additional references, Nature Portfolio reporting summaries, source data, extended data, supplementary information, acknowledgements, peer review information; details of author contributions and competing interests; and statements of data and code availability are available at https://doi.org/10.1038/s41567-022-01844-0.

References

1. Mooij, J. E. & Harmans, C. J. P. M. Phase-slip flux qubits. *New J. Phys.* **7**, 219 (2005).
2. Mooij, J. E. & Nazarov, Yu. V. Superconducting nanowires as quantum phase-slip junctions. *Nat. Phys.* **2**, 169–172 (2006).
3. Liebermann, P. J. & Wilhelm, F. K. Optimal qubit control using single-flux quantum pulses. *Phys. Rev. Appl.* **6**, 024022 (2016).
4. Leonard, E. et al. Digital coherent control of a superconducting qubit. *Phys. Rev. Appl.* **11**, 014009 (2019).
5. Howington, C. et al. Interfacing superconducting qubits with cryogenic logic: readout. *IEEE Trans. Appl. Supercond.* **29**, 1700305 (2019).
6. McDermott, R. et al. Quantum–classical interface based on single flux quantum digital logic. *Quantum Sci. Technol.* **3**, 024004 (2018).
7. Chiorescu, I., Nakamura, Y., Harmans, C. J. P. & Mooij, J. E. Coherent quantum dynamics of a superconducting flux qubit. *Science* **299**, 1869–1871 (2003).
8. Yan, F. et al. The flux qubit revisited to enhance coherence and reproducibility. *Nat. Commun.* **7**, 12964 (2016).
9. Manucharyan, V. E., Koch, J., Glazman, L. I. & Devoret, M. H. Fluxonium: single Cooper-pair circuit free of charge offsets. *Science* **326**, 113–116 (2009).
10. Nguyen, L. B. et al. High-coherence fluxonium qubit. *Phys. Rev. X* **9**, 041041 (2019).

11. Astafiev, O. V. et al. Coherent quantum phase slip. *Nature* **484**, 355–358 (2012).
12. Shaikhaidarov, R. S. et al. Quantized current steps due to the a.c. coherent quantum phase-slip effect. *Nature* **608**, 45–49 (2022).
13. Golubev, D. S. & Zaikin, A. D. Quantum tunneling of the order parameter in superconducting nanowires. *Phys. Rev. B* **64**, 014504 (2001).
14. Sahu, M. et al. Individual topological tunnelling events of a quantum field probed through their macroscopic consequences. *Nat. Phys.* **5**, 503–508 (2009).
15. Tinkham, M. *Introduction to Superconductivity* 2nd edn (Dover, 1996).
16. van Der Wal, C. H. et al. Quantum superposition of macroscopic persistent-current states. *Science* **290**, 773–777 (2000).
17. Friedman, J. R., Patel, V., Chen, W., Tolpygo, S. K. & Lukens, J. E. Quantum superposition of distinct macroscopic states. *Nature* **406**, 43–46 (2000).
18. Likharev, K. K. Superconducting weak links. *Rev. Mod. Phys.* **51**, 101 (1979).
19. Giazotto, F., Peltonen, J. T., Meschke, M. & Pekola, J. P. Superconducting quantum interference proximity transistor. *Nat. Phys.* **6**, 254–259 (2010).
20. Courtois, H., Meschke, M., Peltonen, J. T. & Pekola, J. P. Origin of hysteresis in a proximity Josephson junction. *Phys. Rev. Lett.* **101**, 067002 (2008).
21. Angers, L. et al. Proximity d.c. squids in the long-junction limit. *Phys. Rev. B* **77**, 165408 (2008).
22. Dutta, B. et al. Single-quantum-dot heat valve. *Phys. Rev. Lett.* **125**, 237701 (2020).
23. Schmidt, D. R., Yung, C. S. & Cleland, A. N. Nanoscale radio-frequency thermometry. *Appl. Phys. Lett.* **83**, 1002–1004 (2003).
24. Gasparinetti, S. et al. Fast electron thermometry for ultrasensitive calorimetric detection. *Phys. Rev. Appl.* **3**, 014007 (2015).
25. Karimi, B. & Pekola, J. P. Noninvasive thermometer based on the zero-bias anomaly of a superconducting junction for ultrasensitive calorimetry. *Phys. Rev. Appl.* **10**, 054048 (2018).
26. Karimi, B. et al. Optimized proximity thermometer for ultrasensitive detection. *Phys. Rev. Appl.* **13**, 054001 (2020).
27. Karimi, B., Brange, F., Samuelsson, P. & Pekola, J. P. Reaching the ultimate energy resolution of a quantum detector. *Nat. Commun.* **11**, 367 (2020).
28. Zhou, F., Charlat, P., Spivak, B. & Pannetier, B. Density of states in superconductor-normal metal-superconductor junctions. *J. Low Temp. Phys.* **110**, 841–850 (1998).
29. Le Sueur, H., Joyez, P., Pothier, H., Urbina, C. & Estève, D. Phase controlled superconducting proximity effect probed by tunneling spectroscopy. *Phys. Rev. Lett.* **100**, 197002 (2008).
30. Ligato, N., Strambini, E., Paolucci, F. & Giazotto, F. Preliminary demonstration of a persistent Josephson phase-slip memory cell with topological protection. *Nat. Commun.* **12**, 5200 (2021).
31. Larkin, A. L. & Ovchinnikov, Yu. N. Quasiclassical method in the theory of superconductivity. *Zh. Eksp. Teor. Fiz.* **55**, 2262–2272 (1968).
32. Usadel, K. D. Generalized diffusion equation for superconducting alloys. *Phys. Rev. Lett.* **25**, 507 (1970).
33. Belzig, W., Wilhelm, F. K., Bruder, C., Schön, G. & Zaikin, A. D. Quasiclassical Green's function approach to mesoscopic superconductivity. *Superlattices Microstruct.* **25**, 1251 (1999).
34. Giazotto, F., Heikkilä, T. T., Luukanen, A., Savin, A. M. & Pekola, J. P. Opportunities for mesoscopics in thermometry and refrigeration: physics and applications. *Rev. Mod. Phys.* **78**, 217 (2006).
35. Viisanen, K. L. & Pekola, J. P. Anomalous electronic heat capacity of copper nanowires at sub-kelvin temperatures. *Phys. Rev. B* **97**, 115422 (2018).
36. Wang, L. B., Golubev, D. S., Galperin, Y. M. & Pekola, J. P. Dynamic thermal relaxation in metallic films at sub-kelvin temperatures. Preprint at https://arxiv.org/abs/1910.09448 (2019).
37. Pekola, J. P. & Karimi, B. Ultrasensitive calorimetric detection of single photons from qubit decay. *Phys. Rev. X* **12**, 011026 (2022).
38. Braine, T. et al. Extended search for the invisible axion with the axion dark matter experiment. *Phys. Rev. Lett.* **124**, 101303 (2020).

Methods

Sample fabrication

First, we pattern the RFL on an intrinsic Si waver by evaporating a Nb thin film of thickness 100 nm under ultrahigh vacuum conditions. The Nb is covered in situ with a 5 nm silicon layer, to avoid surface degradation. An Al etch mask is elaborated using electron-beam lithography and lift-off on top of the Nb, through which the 500-nm-wide RFL is patterned using reactive ion etching.

In the second step, the RF-SQUIPT is elaborated using a double-layer resist and a three-angle metallic thin-film evaporation. The angular rotation axis is taken parallel to the RFL. First, we deposit 25 nm of Al at an angle of −38° from normal incidence, which is oxidized in situ under a controlled oxygen pressure of 0.25 mbar during 5 s. This allows growing the tunnel barrier for the thermometer junction. The next layer consists of 35 nm of Cu at zero angle. Finally, we evaporate 60 nm of Al at an angle of +38°, which provides the main superconducting SQUID loop. The superconducting loop is aligned with respect to the RFL such as to have a separation of about 2 µm along the parallel edges.

The superconducting RF resonators[24] are located on a physically separate chip, adjacent to the sample chip and connected to the sample via several Al microbondings in parallel. The circuit elements are made of Al (100 nm thick) fabricated via laser lithography followed by physical vapour deposition.

Data availability

The datasets plotted in this work are available via Zenodo at https://zenodo.org/record/6389955. The raw datasets are large files and can be obtained from the corresponding author upon request.

Author contributions

E.G. performed the experiments, with the help of P.R. D.M. prepared the samples, with the help of E.G. and P.R. D.N. and W.B. performed the theoretical modelling. B.K., J.T.P. and J.P.P. developed and helped installing the RF thermometry methods. E.G. and C.B.W. conceived the experiment. C.B.W. conducted the research and wrote the manuscript, with input from all the authors. All the authors contributed to the discussions and interpretation of data.

Competing interests

The authors declare no competing interests.

Additional information

Supplementary information The online version contains supplementary material available at https://doi.org/10.1038/s41567-022-01844-0.

Correspondence and requests for materials should be addressed to C. B. Winkelmann.

Peer review information *Nature Physics* thanks the anonymous reviewers for their contribution to the peer review of this work

Reprints and permissions information is available at www.nature.com/reprints.